Stability Analysis and Enhanced Virtual Synchronous Control for Brushless Doubly-fed Induction Generator Based Wind Turbines

Hailiang Xu, Chao Wang, Zhongxing Wang, Pingjuan Ge, and Rende Zhao

***Abstract*—The brushless doubly-fed induction generator (BDFIG) presents significant potential for application in wind power systems, primarily due to the elimination of slip rings and brushes. The application of virtual synchronous control (VSynC) has been demonstrated to effectively augment the inertia of BDFIG systems. However, the dynamic characteristics and stability of BDFIG under weak grid conditions remain largely unexplored. The critical stabilizing factors for BDFIG-based wind turbines (WTs) are methodically investigated, and an enhanced VSynC method based on linear active disturbance rejection control (LADRC) is proposed. The stability analysis reveals that the proposed method can virtually enhance the stability of the grid-connected system under weak grid conditions. The accuracy of the theoretical analysis and the effectiveness of the proposed method are affirmed through extensive simulations and detailed experiments.**

***Index Terms*—Brushless doubly-fed induction generator (BDFIG), virtual synchronous control (VSynC), stability analysis, linear active disturbance rejection control (LADRC).**

NOMENCLATURE

$\boldsymbol{\psi}_p$, $\boldsymbol{\psi}_c$, $\boldsymbol{\psi}_r$	Vectors of power winding (PW), control winding (CW) and rotor winding (RW) magnetic flux
σ	Overshoot value
ω	Angular velocity of grid
ω_0	Synchronous angular velocity of grid
ω_p	PW angular velocity
ω_r	RW angular velocity
ω_c	CW angular velocity
$\tilde{\theta}_p$	Grid voltage angle perturbation
θ_p	Grid voltage angle
θ_r	RW angle
θ_{slip}	Angular aberration
Δi_{cd}, Δi_{cq}	d- and q-axis CW current compensations
ΔP_{out}	Deviation value of outturn active power
ΔP_{ref}	Deviation value of reference active power
β_1, β_2	Observer gains
b_0	Known part of control gain b
$b_{0,i}$	Current of b_0
$C_1(s)$	Closed-loop feedback controller
$C_f(s)$	Closed-loop feedforward controller
D	Virtual damping coefficient
E_0	Rated grid voltage value
$\boldsymbol{E}_1$	Identity matrix
E	Reference grid voltage amplitude
f_{total}	Sum of system perturbations
$\boldsymbol{G}_{ipp}$	Transfer function matrix between PW voltage and current
$\boldsymbol{G}_p$	Control object
$\boldsymbol{G}_{pr}$	Transfer function matrix between PW and RW currents
$\boldsymbol{G}_{rc}$	Transfer function matrix between RW and CW currents
$\boldsymbol{G}_{cr}$	Transfer function matrix between CW and RW currents
$\boldsymbol{G}_{cu}$	Transfer function matrix of voltage control loop
$\boldsymbol{G}_{ci}$	Transfer function matrix of current control loop
$\boldsymbol{G}_{irp}$	Transfer function matrix between RW voltage and PW current
$\boldsymbol{G}_{icc}$	Transfer function matrix between CW voltage and current
$\boldsymbol{G}_{pq}^{u}$, $\boldsymbol{G}_{pq}^{i}$	Transfer function matrices of q-axis voltage and current coordinate transformation
$\boldsymbol{G}_p^d$	Transfer function matrix of d-axis virtual synchronization control
$\boldsymbol{G}_{up}^d$	Transformer transfer function matrix of d-axis PW voltage
$\tilde{i}_{pd}$, $\tilde{i}_{pq}$	d- and q-axis PW current disturbances
$\tilde{\boldsymbol{i}}_p$, $\tilde{\boldsymbol{i}}_r$	Vectors of PW and RW current disturbances

Manuscript received: July 17, 2023; revised: September 24, 2023; accepted: December 25, 2023. Date of CrossCheck: December 25, 2023. Date of online publication: February 2, 2024.

This work was supported by the National Natural Science Foundation of China (No. 52077222) and the Shandong Provincial Natural Science Foundation (No. ZR2023QE156).

H. Xu, C. Wang, Z. Wang, P. Ge (corresponding author), and R. Zhao are with China University of Petroleum (East China), Qingdao 266580, China (e-mail: xuhl@upc.edu.cn; 1806030518@s.upc.edu.cn; s20150044@s.upc.edu.cn; gepingjuan@upc.edu.cn; zhaorende@upc.edu.cn).

DOI: 10.35833/MPCE.2023.000482

$\tilde{\boldsymbol{i}}_{\mathrm{c}}$, $\tilde{\boldsymbol{i}}_{\mathrm{c,ref}}$	Vectors of CW current disturbance and its reference
$\boldsymbol{i}_{\mathrm{p}}$, $\boldsymbol{i}_{\mathrm{c}}$, $\boldsymbol{i}_{\mathrm{r}}$	Vectors of PW, CW, and RW currents
i_{cd}, i_{cq}	d- and q-axis CW currents
$i_{cd,\mathrm{err}}$, $i_{cq,\mathrm{err}}$	d- and q-axis CW current discrepancies
i_{pd}, i_{pq}	d- and q-axis PW currents
I_{pd}, I_{pq}	Steady-state values of d- and q-axis PW currents
J	Virtual inertia coefficient
k_{p}	Error feedback coefficient
K_{ω}	Primary frequency modulation coefficient
K_{pu}, K_{iu}	Proportional and integral coefficients of voltage loop
K_{pi}, K_{ii}	Proportional and integral coefficients of current loop
L_{p}, L_{c}, L_{r}	PW, CW, and RW self-inductances
L_{M}	Mechanical inductance
M_{pr}	Mutual inductance between PW and RW
M_{cr}	Mutual inductance between CW and RW
n	Droop coefficient
P	Output active power
P_{m}	Input virtual mechanical power
P_{e}	Output electromagnetic active power
P_{ref}	Reference active power
$P_{\mathrm{p,ref}}$	PW reference active power
$\tilde{P}_{\mathrm{p}}$	PW active power disturbance
Q_{ref}	Reference reactive power
$Q_{\mathrm{p,ref}}$	PW reference reactive power
Q	Output electromagnetic reactive power
$\tilde{Q}_{\mathrm{p}}$	PW reactive power disturbance
R_{p}, R_{c}, R_{r}	PW, CW, and RW resistances
R_{g}, L_{g}	Resistance and inductance of grid
u	Control input quantity
u_0	Output of linear state error feedback (LSEF)
u_{pd}, u_{pq}	d- and q-axis PW voltages
u_{cd}, u_{cq}	d- and q-axis CW voltages
$u_{pd,\mathrm{err}}$, $u_{pq,\mathrm{err}}$	d- and q-axis PW voltage discrepancies
$\boldsymbol{u}_{\mathrm{p}}$, $\boldsymbol{u}_{\mathrm{c}}$, $\boldsymbol{u}_{\mathrm{r}}$	PW, CW, and RW voltage vectors
$\tilde{\boldsymbol{u}}_{\mathrm{p}}$, $\tilde{\boldsymbol{u}}_{\mathrm{p,ref}}$	Vectors of PW voltage disturbance and its reference
$\tilde{u}_{pd}$, $\tilde{u}_{pq}$	d- and q-axis PW voltage disturbances
$\tilde{\boldsymbol{u}}_{\mathrm{c}}$, $\tilde{\boldsymbol{u}}_{\mathrm{c,ref}}$	Vectors of CW voltage disturbance and its reference
U_{pd}, U_{pq}	Steady-state values of d- and q-axis PW voltages
U_{p}, U_{g}	PW voltage and grid voltage amplitudes
U_{s}	Stator voltage
U_{ref}	PW reference voltage
$\tilde{U}_{\mathrm{p}}$	PW voltage amplitude disturbance
v	Reference of LSEF input
$\tilde{\boldsymbol{x}}$	Small-signal disturbance matrix of brushless doubly-fed induction generator (BDFIG) system
$\tilde{x}_d$, $\tilde{x}_q$	d- and q-axis disturbances
X, R	Equivalent reactance and resistance
$\boldsymbol{Y}(s)$	Matrix of BDFIG system admittance
$\boldsymbol{Y}_{\mathrm{open\text{-}loop}}^{\mathrm{BDFIG}}$	Transfer function matrix of open-loop admittance of BDFIG system
$\boldsymbol{Y}_{\mathrm{BDFIG}}$	Transfer function matrix of admittance of BDFIG system
z_1	Real-time observation of output quantity of BDFIG system y
z_2	Estimate of real-time observation of internal and external disturbances
$\boldsymbol{Z}_{\mathrm{g}}(s)$	Matrix of grid impedance

I. Introduction

AMONG the various types of grid-connected wind turbines (WTs), the doubly-fed induction generator (DFIG) is often preferred [1]. However, it faces significant reliability issues under harsh conditions such as sand and dust storms, high humidity, and environments with elevated salt content, primarily due to the high failure rate of its slip rings and brushes. In contrast, the brushless DFIG (BDFIG) emerges as a compelling alternative, and its unique machine structure can notably eliminate slip rings and brushes [2]-[5].

However, with the increasing integration of power electronics-based renewable energy sources, the inertia and damping characteristics of power systems are progressively diminishing [6]. As a result, the stability of the power system is increasingly compromised [7]. This particularly exacerbates the stability of the power system [8]. To settle such issues, the virtual synchronous control (VSynC) approach has been generally recognized as an effective solution to enhance the inertia characteristic of the power electronics-based system [9]. The VSynC approach enables WTs to emulate the frequency response of traditional synchronous generators (SGs), thereby mitigating the impact of grid-connected WTs on the frequency stability of the AC power system [10], [11]. This is especially crucial when the short-circuit ratio (SCR) of the power system is low, because the control method based on conventional phase-locked loop (PLL) can lead to instability [12]. In contrast, the VSynC approach is capable of enhancing both the inertia and damping of the power system, offering a more stable and reliable solution [13].

For instance, the VSynC approaches have been employed in WTs to enhance the inertia support capability [14]-[18]. In [14], the output impedance of DFIG based on VSynC is constructed for the stability analysis of the AC power system. An enhanced VSynC for grid-connected converters operating under unbalanced grid conditions is introduced, although it lacks an analysis of the impact of crucial control parameters and grid strength on the stability of the power system in [15]. A robust method to articulate the inertial dynamics of DFIG based on VSynC is offered in [16], validating the electromechanical motion equation of WTs. In addition, a comprehensive WT controller is proposed, integrating inertial response and frequency regulation for rapid virtual inertia under load shedding conditions [17]. An enhanced control method for virtual synchronous generator (VSG) by

dynamically varying droop coefficients are proposed to expand the stability margin of the DFIG system in [18]. Notably, the power electronics-based VSynC may face instability risks under weak grid conditions [19].

To tackle this challenge, a linear active disturbance rejection control (LADRC) is employed for a standard three-phase grid-connected converter, as demonstrated in [20]. This application suggests a substantial enhancement of the stability of the power system. Furthermore, [21] discovers that LADRC offers superior adaptability to weak grid conditions and can significantly outperform the traditional proportional-integral (PI) controller in enhancing the stability of the power system. The current methodologies for modeling and stability analysis of the DFIG system offer insightful references for studying the stability of BDFIG systems [22].

Nevertheless, the stability analysis of the BDFIG system is more challenging, owing to its complex machine structure. Most of the previous studies on control methods of BDFIG system generally fall into two categories, which are the field-/voltage-oriented vector control (VC) [23] and direct power control/torque control (DPC/DTC) [24]. In [23], a VC method of BDFIG operating as a variable speed generator is proposed, controlling the speed and reactive power simultaneously. In [24], a DPC method based on backstepping for a dual-cage rotor BDFIG is presented. Unfortunately, these methods lack inherent frequency regulation capabilities for BDFIG-based WTs. In [25], the integration of VSynC in the BDFIG system not only enables inertia support to the grid, but also enhances the grid transient performance during voltage dips. Despite these advancements, there is still a notable gap on the stability of BDFIG system with enhanced VSynC, particularly in terms of small-signal stability assessment. The primary challenges are: ① the complex modeling of the BDFIG and the unexplored impact of the VSynC on its impedance characteristics; ② the unclear influence of critical VSynC parameters on BDFIG performance under weak grid conditions; and ③ the absence of robust methods to reinforce the stability margin of BDFIG systems with enhanced VSynC under weak grid conditions.

Addressing these challenges, the critical stabilizing factors crucial for BDFIG-based WTs are methodically investigated, and an enhanced VSynC method based on LADRC is proposed to enhance the stability of the BDFIG system. The accuracy of the theoretical analysis and the effectiveness of the proposed method are affirmed through extensive simulations and detailed experiments.

II. BDFIG with Enhanced VSynC and Impedance Characteristic Analysis

A. BDFIG with Enhanced VSynC

The topology and control structure of BDFIG system are shown in Fig. 1 [4], [5]. The BDFIG system has two kinds of windings, namely the power winding (PW) with a pole pair p_p and the control winding (CW) with a pole pair p_c. The magnetic pole pair of the rotor winding (RW) is p_p+p_c. Similar to the traditional DFIG system, the machine-side converter (MSC) of BDFIG is connected to the CW. The MSC is controlled by space vector pulse width modulation (SVPWM). As depicted in Fig. 1, the VSynC is implemented within the BDFIG system.

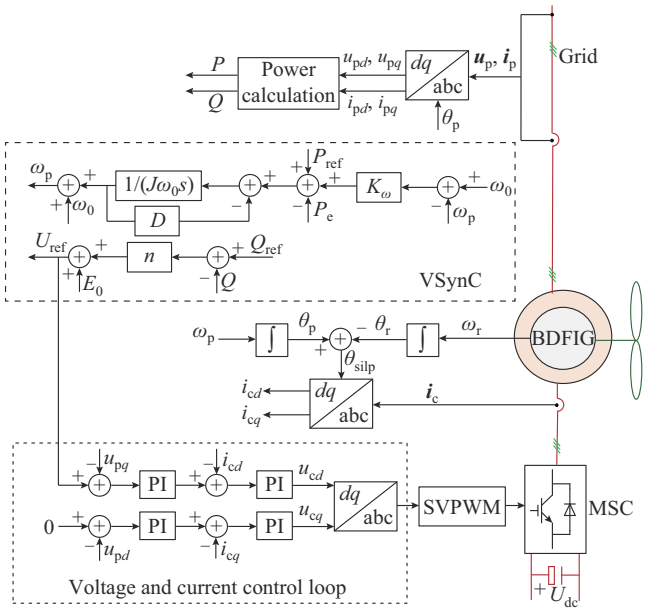

Fig. 1. Topology and control structure of BDFIG system.

When employing the VSynC, the BDFIG system acquires inertia and damping properties, enabling it to emulate the output characteristics of traditional SGs. The power outer control loop includes the active power control loop and reactive power control loop.

The active power control loop can be expressed as:

$$P_m - P_e - D(\omega_0 - \omega) = J\omega \frac{d\omega}{dt} \approx J\omega_0 \frac{d\omega}{dt} \tag{1}$$

P_m contains two components, namely the reference active power and the output of the virtual functionary, which can be expressed as:

$$P_m = P_{ref} + K_\omega(\omega_0 - \omega) \tag{2}$$

Similarly, the reactive power control can be expressed as:

$$U_{ref} = E_0 + n(Q_{ref} - Q) \tag{3}$$

B. Impedance Characteristics of BDFIG System

1) BDFIG System Modeling

In the synchronous coordinate system, the voltage and magnetic equations of BDFIG system can be obtained as [3], [4]:

$$\begin{cases} \boldsymbol{u}_p = R_p \boldsymbol{i}_p + \dot{\boldsymbol{\psi}}_p + j\omega_p \boldsymbol{\psi}_p \\ \boldsymbol{u}_c = R_c \boldsymbol{i}_c + \dot{\boldsymbol{\psi}}_c + j\omega_c \boldsymbol{\psi}_c \\ \boldsymbol{u}_r = R_r \boldsymbol{i}_r + \dot{\boldsymbol{\psi}}_r + j\omega_r \boldsymbol{\psi}_r \\ \boldsymbol{\psi}_p = L_p \boldsymbol{i}_p + M_{pr} \boldsymbol{i}_r \\ \boldsymbol{\psi}_c = L_c \boldsymbol{i}_c + M_{cr} \boldsymbol{i}_r \\ \boldsymbol{\psi}_r = L_r \boldsymbol{i}_r + M_{pr} \boldsymbol{i}_p + M_{cr} \boldsymbol{i}_c \end{cases} \tag{4}$$

where $\omega_r = \omega_p - \dot{\omega}_m$, ω_m is the mechanical angular velocity; and $\dot{(\cdot)}$ is the differential operator.

PW and CW voltages are taken as input variables, and the

currents are taken as output variables. The open-loop input admittance model of BDFIG system is established, as shown in Fig. 2.

$$\begin{cases} \tilde{\boldsymbol{x}}=[\tilde{x}_d \quad \tilde{x}_q]^{\mathrm{T}} \\ \boldsymbol{x}=[\boldsymbol{u}_{\mathrm{p}} \ \boldsymbol{u}_{\mathrm{c}} \ \boldsymbol{i}_{\mathrm{p}} \ \boldsymbol{i}_{\mathrm{c}}] \\ \tilde{\boldsymbol{i}}_{\mathrm{p}}=\boldsymbol{G}_{\mathrm{ipp}}\tilde{\boldsymbol{u}}_{\mathrm{p}}+\boldsymbol{G}_{\mathrm{pr}}\tilde{\boldsymbol{i}}_{\mathrm{r}} \\ \tilde{\boldsymbol{i}}_{\mathrm{c}}=\boldsymbol{G}_{\mathrm{icc}}\tilde{\boldsymbol{u}}_{\mathrm{c}}+\boldsymbol{G}_{\mathrm{cr}}\tilde{\boldsymbol{i}}_{\mathrm{r}} \\ \tilde{\boldsymbol{i}}_{\mathrm{r}}=\boldsymbol{G}_{\mathrm{irp}}\tilde{\boldsymbol{u}}_{\mathrm{p}}+\boldsymbol{G}_{\mathrm{rc}}\tilde{\boldsymbol{i}}_{\mathrm{c}} \end{cases} \tag{5}$$

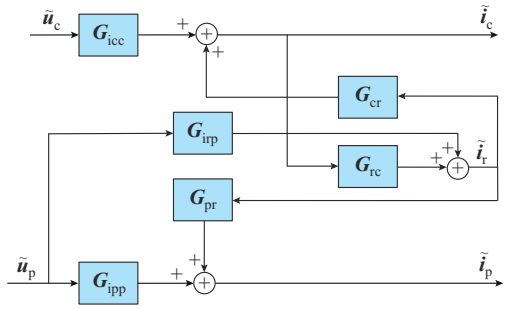

Fig. 2. Open-loop input admittance model of BDFIG system.

Simplifying the transfer functions in Fig. 2, the detailed derivation processes are given as (A1)-(A9) in Appendix A. The simplified open-loop input admittance model of BDFIG is shown in Appendix A Fig. A1 and the expression of the open-loop admittance of the BDFIG system can be obtained as:

$$\boldsymbol{Y}_{\text{open-loop}}^{\text{BDFIG}}=\frac{\boldsymbol{G}_{\mathrm{pr}}}{\boldsymbol{E}_1-\boldsymbol{G}_{\mathrm{rc}}\boldsymbol{G}_{\mathrm{cr}}}\boldsymbol{G}_{\mathrm{irp}}+\boldsymbol{G}_{\mathrm{ipp}} \tag{6}$$

2) Voltage Control Loop and Current Control Loop Modeling

From the mathematical model of the BDFIG system, the relation between the CW and PW currents can be obtained. Under the *d*-axis orientation of the PW magnetic flux, the relation can be re-written as:

$$\begin{cases} i_{cd}=\dfrac{R_{\mathrm{r}}L_{\mathrm{p}}}{\omega_{\mathrm{p}}M_{\mathrm{cr}}M_{\mathrm{pr}}}i_{pq}+\dfrac{L_{\mathrm{M}}}{\omega_{\mathrm{p}}M_{\mathrm{cr}}}\dot{i}_{pq}+\Delta i_{cd} \\ i_{cq}=-\dfrac{R_{\mathrm{r}}L_{\mathrm{p}}}{\omega_{\mathrm{p}}M_{\mathrm{cr}}M_{\mathrm{pr}}}i_{pd}+\dfrac{L_{\mathrm{M}}}{\omega_{\mathrm{p}}M_{\mathrm{cr}}}\dot{i}_{pd}+\Delta i_{cq} \\ \Delta i_{cd}=\dfrac{L_{\mathrm{M}}}{M_{\mathrm{cr}}}i_{pd}-\dfrac{L_{\mathrm{r}}}{M_{\mathrm{cr}}M_{\mathrm{pr}}}\psi_{\mathrm{p}}+\dfrac{1}{\omega_{\mathrm{p}}}\dot{i}_{cq} \\ \Delta i_{cq}=-\dfrac{L_{\mathrm{M}}}{M_{\mathrm{cr}}}i_{pq}+\dfrac{R_{\mathrm{r}}+L_{\mathrm{r}}}{\omega_{\mathrm{p}}M_{\mathrm{cr}}M_{\mathrm{pr}}}\psi_{\mathrm{p}}-\dfrac{1}{\omega_{\mathrm{p}}}\dot{i}_{cd} \end{cases} \tag{7}$$

where $L_{\mathrm{M}}=L_{\mathrm{r}}L_{\mathrm{p}}/M_{\mathrm{pr}}-M_{\mathrm{pr}}$.

It can be observed from (7) that the PW magnetic flux ψ_{p} basically keeps constant under the stable condition. Besides, the changing rates of both the PW current and voltage are approximately first-order linear. Neglecting the coupling term, the equation of voltage control can be derived as:

$$\begin{cases} i_{cd}=\left(K_{\mathrm{pu}}+\dfrac{K_{\mathrm{iu}}}{s}\right)u_{pq,\mathrm{err}} \\ i_{cq}=\left(K_{\mathrm{pu}}+\dfrac{K_{\mathrm{iu}}}{s}\right)u_{pd,\mathrm{err}} \end{cases} \tag{8}$$

Thus, the voltage control loop can be disclosed as:

$$\tilde{\boldsymbol{i}}_{\mathrm{c}}=\begin{bmatrix} K_{\mathrm{pu}}+\dfrac{K_{\mathrm{iu}}}{s} & 0 \\ 0 & K_{\mathrm{pu}}+\dfrac{K_{\mathrm{iu}}}{s} \end{bmatrix}\tilde{\boldsymbol{u}}_{\mathrm{p}} \tag{9}$$

Typically, when the PI regulator is used in the current control loop, u_{cd} and u_{cq} can be expressed as:

$$\begin{cases} u_{cd}=\left(K_{\mathrm{pi}}+\dfrac{K_{\mathrm{ii}}}{s}\right)i_{cd,\mathrm{err}}-\omega_{\mathrm{c}}\left(L_{\mathrm{c}}i_{cq}-\dfrac{L_{\mathrm{p}}M_{\mathrm{cr}}}{M_{\mathrm{pr}}}i_{pq}\right) \\ u_{cq}=\left(K_{\mathrm{pi}}+\dfrac{K_{\mathrm{ii}}}{s}\right)i_{cq,\mathrm{err}}+\omega_{\mathrm{c}}\left(L_{\mathrm{c}}i_{cd}-\dfrac{L_{\mathrm{p}}M_{\mathrm{cr}}}{M_{\mathrm{pr}}}i_{pd}\right) \end{cases} \tag{10}$$

Thus, the current control loop can be obtained as:

$$\tilde{\boldsymbol{u}}_{\mathrm{c}}=\begin{bmatrix} K_{\mathrm{pi}}+\dfrac{K_{\mathrm{ii}}}{s} & 0 \\ 0 & K_{\mathrm{pi}}+\dfrac{K_{\mathrm{ii}}}{s} \end{bmatrix}\tilde{\boldsymbol{i}}_{\mathrm{c}} \tag{11}$$

3) VSynC Loop Modeling

In the synchronous coordinate system, the active and reactive power references of the PWs under steady state can be denoted as $P_{\mathrm{p,ref}}$ and $Q_{\mathrm{p,ref}}$, respectively. The calculation of $P_{\mathrm{p,ref}}$ and $Q_{\mathrm{p,ref}}$ are given by (B1) in Appendix B. Injecting a small-signal perturbation under the steady-state working point yields (refer to Appendix B (B1) for detailed derivation process):

$$\begin{cases} P_{\mathrm{p,ref}}+\tilde{P}_{\mathrm{p}}=-\dfrac{3[(I_{pd}+\tilde{i}_{pd})(U_{pd}+\tilde{u}_{pd})+(I_{pq}+\tilde{i}_{pq})(U_{pq}+\tilde{u}_{pq})]}{2} \\ Q_{\mathrm{p,ref}}+\tilde{Q}_{\mathrm{p}}=-\dfrac{3[(I_{pd}+\tilde{i}_{pd})(U_{pq}+\tilde{u}_{pq})-(I_{pq}+\tilde{i}_{pd})(U_{pq}+\tilde{u}_{pd})]}{2} \end{cases} \tag{12}$$

Then, the above equation is expanded and the steady-state values are eliminated, which can be expressed as:

$$\begin{cases} \begin{bmatrix} \tilde{P}_{\mathrm{p}} \\ \tilde{Q}_{\mathrm{p}} \end{bmatrix}=\boldsymbol{G}_{pq}^{\mathrm{u}}\tilde{\boldsymbol{u}}_{\mathrm{p}}+\boldsymbol{G}_{pq}^{\mathrm{i}}\tilde{\boldsymbol{i}}_{\mathrm{p}} \\ \boldsymbol{G}_{pq}^{\mathrm{u}}=-\dfrac{3}{2}\begin{bmatrix} U_{pd} & U_{pq} \\ U_{pq} & -U_{pd} \end{bmatrix} \\ \boldsymbol{G}_{pq}^{\mathrm{i}}=-\dfrac{3}{2}\begin{bmatrix} I_{pd} & I_{pq} \\ -I_{pq} & I_{pd} \end{bmatrix} \end{cases} \tag{13}$$

The simplified structure of VSynC loop is illustrated in Fig. 3.

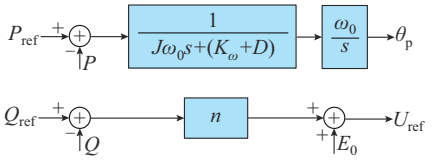

Fig. 3. Simplified structure of VSynC loop.

Setting the small-signal perturbation of the active and reactive power as the input, the phase and amplitude can be derived as:

$$\begin{cases}\begin{bmatrix}\tilde{\theta}_{\mathrm{p}}\\ \tilde{U}_{\mathrm{p}}\end{bmatrix}=\boldsymbol{G}_{\mathrm{pq}}^{d}\begin{bmatrix}P_{\mathrm{p,ref}}-\tilde{P}_{\mathrm{p}}\\ Q_{\mathrm{p,ref}}-\tilde{Q}_{\mathrm{p}}\end{bmatrix}\\ \boldsymbol{G}_{\mathrm{p}}^{d}=\begin{bmatrix}\dfrac{\omega_0}{s(J\omega_0 s+K_\omega+D)} & 0\\ 0 & n\end{bmatrix}\end{cases}\tag{14}$$

Then, the PW voltage to the synchronous coordinate system is converted, which can be expressed as:

$$\begin{cases}u_{pd}=|\boldsymbol{u}_{\mathrm{p}}|\cos\theta_{\mathrm{p}}\\ u_{pq}=|\boldsymbol{u}_{\mathrm{p}}|\sin\theta_{\mathrm{p}}\end{cases}\tag{15}$$

Linearizing (15) via the small signal, we can obtain:

$$\begin{cases}\tilde{\boldsymbol{u}}_{\mathrm{p,ref}}=\boldsymbol{G}_{\mathrm{up}}^{d}[\tilde{\theta}_{\mathrm{p}}\quad\tilde{U}_{\mathrm{p}}]^{\mathrm{T}}\\ \boldsymbol{G}_{\mathrm{up}}^{d}=\begin{bmatrix}-u_{\mathrm{p0}}\sin\theta_{\mathrm{p0}} & \cos\theta_{\mathrm{p0}}\\ u_{\mathrm{p0}}\cos\theta_{\mathrm{p0}} & \sin\theta_{\mathrm{p0}}\end{bmatrix}\end{cases}\tag{16}$$

where subscript 0 is the corresponding small-signal variable.

Combining (14) and (16), the vector of PW voltage disturbance reference can be expressed as:

$$\tilde{\boldsymbol{u}}_{\mathrm{p,ref}}=\boldsymbol{G}_{\mathrm{up}}^{d}\boldsymbol{G}_{\mathrm{pq}}^{d}\begin{bmatrix}P_{\mathrm{p,ref}}-\tilde{P}_{\mathrm{p}}\\ Q_{\mathrm{p,ref}}-\tilde{Q}_{\mathrm{p}}\end{bmatrix}\tag{17}$$

Combining (5)-(17), the complete input admittance model of BDFIG system with VSynC can be summarized as in Fig. 4, and the detailed admittance of BDFIG system can be expressed as:

$$\begin{cases}\boldsymbol{Y}_{\mathrm{BDFIG}}=\dfrac{\boldsymbol{G}_{\mathrm{ipp}}+\boldsymbol{G}_{\mathrm{irp}}\boldsymbol{G}_5+\boldsymbol{G}_3\boldsymbol{G}_2\boldsymbol{G}_5}{\boldsymbol{E}_1+\boldsymbol{G}_4\boldsymbol{G}_2\boldsymbol{G}_5}\\ \boldsymbol{G}_1=\dfrac{\boldsymbol{G}_{\mathrm{cr}}}{\boldsymbol{G}_{\mathrm{cu}}\boldsymbol{G}_{\mathrm{ci}}\boldsymbol{G}_{\mathrm{icc}}}\\ \boldsymbol{G}_2=\dfrac{\boldsymbol{G}_{\mathrm{cu}}\boldsymbol{G}_{\mathrm{ci}}\boldsymbol{G}_{\mathrm{icc}}\boldsymbol{G}_{\mathrm{rc}}}{\boldsymbol{E}_1+\boldsymbol{G}_{\mathrm{ci}}\boldsymbol{G}_{\mathrm{icc}}}\\ \boldsymbol{G}_3=\boldsymbol{G}_{\mathrm{pq}}^{\mathrm{u}}\boldsymbol{G}_{\mathrm{pq}}^{d}\boldsymbol{G}_{\mathrm{up}}^{d}-\boldsymbol{E}_1\\ \boldsymbol{G}_4=\boldsymbol{G}_{\mathrm{pq}}^{\mathrm{i}}\boldsymbol{G}_{\mathrm{pq}}^{d}\boldsymbol{G}_{\mathrm{up}}^{d}\\ \boldsymbol{G}_5=\dfrac{\boldsymbol{G}_{\mathrm{pr}}}{\boldsymbol{E}_1-\boldsymbol{G}_1\boldsymbol{G}_2}\end{cases}\tag{18}$$

Accordingly, the frequency response curves of the BDFIG are obtained. The bode diagram of output admittance of the BDFIG system is shown in Fig. 5. As can be discovered, the output admittance characteristics at the frequency band above 50 Hz almost overlap with each other. However, in the frequency band below 50 Hz, the output impedance characteristics are distinguished. It can be inferred that the VSynC loop mainly influences the impedance characteristics within low frequency band of the BDFIG system.

III. Key Stabilizing Factors of BDFIG System with VSynC

A. Influencing Law of VSynC

According to the developed input model, the BDFIG system behaves as multi-input multi-output characteristic in the *dq* coordinate. According to the generalized Nyquist criterion theorem, the stability of the BDFIG system can be estimated by the total time number of the loop matrix that wraps around (–1, 0).

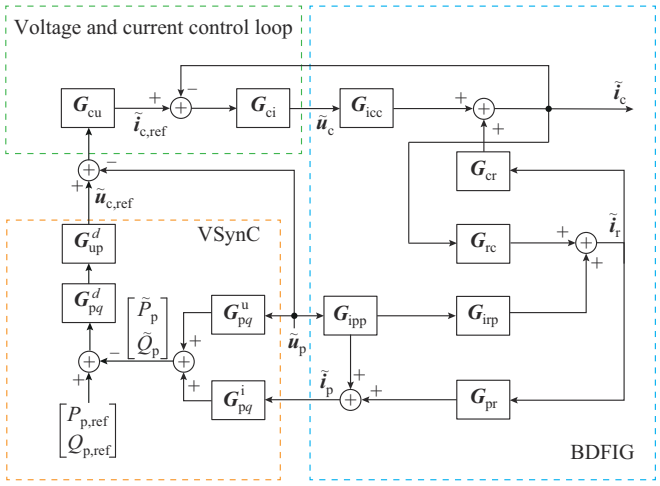

Fig. 4. Model of BDFIG system with VSynC.

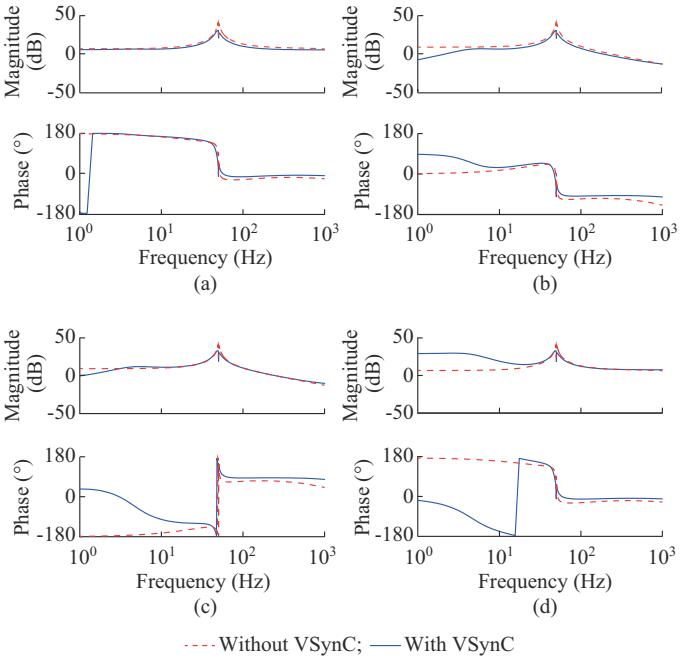

Fig. 5. Bode diagram of output admittance of BDFIG system. (a) *d*-axis component. (b) *d*- and *q*-axis coupled components. (c) *q*- and *d*-axis coupled components. (d) *q*-axis component.

For the BDFIG system, the loop matrix $\boldsymbol{L}(s)$ can be expressed as $\boldsymbol{L}(s)=\boldsymbol{Z}_{\mathrm{g}}(s)\boldsymbol{Y}(s)$.

$$\boldsymbol{Z}_{\mathrm{g}}(s)=\begin{bmatrix}R_{\mathrm{g}}+sL_{\mathrm{g}} & -\omega L_{\mathrm{g}}\\ \omega L_{\mathrm{g}} & R_{\mathrm{g}}+sL_{\mathrm{g}}\end{bmatrix}\tag{19}$$

As shown in Fig. 6, it is assumed that the output voltage of the BDFIG system is $U_{\mathrm{p}}\angle\theta$, while the grid voltage is $U_{\mathrm{g}}\angle 0°$, and the grid impedance is $Z\angle\delta=R+\mathrm{j}X$. Then, the output power of the BDFIG system can be expressed as:

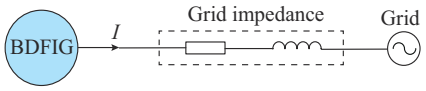

Fig. 6. Structure diagram of BDFIG system connected to grid.

$$\begin{cases} P=\dfrac{U_g}{Z[(U_p\cos\theta-U_g)\cos\delta+U_p\sin\delta\sin\theta]} \\ Q=\dfrac{U_g}{Z[(U_p\cos\theta-U_g)\sin\delta-U_p\cos\delta\sin\theta]} \end{cases} \tag{20}$$

Considering that the value of the equivalent resistance R is much smaller than that of the equivalent reactance X, the grid impedance angle can be assumed to be $\psi=90°$. Then, the output power is approximated as:

$$\begin{cases} P=\dfrac{U_pU_g}{X}\cos\theta \\ Q=\dfrac{U_p(U_p-U_g)}{X} \end{cases} \tag{21}$$

According to (21), the active power-frequency loop $G(s)$ can be conveyed as:

$$G(s)=\frac{\Delta P_{out}}{\Delta P_{ref}}=\frac{\dfrac{U_pU_g}{X}}{J\omega_0 s^2+(K_\omega+D)s+\dfrac{U_pU_g}{X}} \tag{22}$$

From (22), the damping ratio ξ and the natural oscillation frequency ω_n are obtained as:

$$\begin{cases} \xi=\dfrac{(K_\omega+D)\sqrt{Z}}{2\sqrt{U_sU_gJ\omega_0}} \\ \omega_n=\sqrt{\dfrac{U_pU_g}{J\omega_0 Z}} \end{cases} \tag{23}$$

The three-dimensional relationship among J, D, and ξ is shown in Fig. 7. The damping ratio is set to be $0.7<\xi<1.0$ to avoid excessive frequency fluctuation that would endanger the stable operation of the system. As illustrated in Fig. 7, reducing J or augmenting D contributes to a higher damping ratio, thereby enhancing the stability of the system.

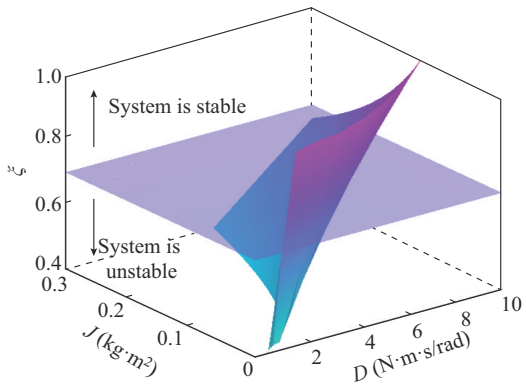

Fig. 7. Three-dimensional relationship among J, D, and ξ.

According to (22), the open-loop transfer function $G_0(s)$ can be demonstrated as:

$$G_0(s)=\frac{U_pU_g}{Z}\frac{1}{s(J\omega_0 s+K_\omega+D)} \tag{24}$$

Setting $1+G_0(s)=0$, the root trajectories of the grid-connected system can be derived as:

$$s^2+\frac{D+K_\omega}{J\omega_0}s+\frac{1}{J\omega_0}\frac{U_pU_g}{Z}=0 \tag{25}$$

Based on (25), the root trajectories of the system under different J and D can be obtained, as shown in Fig. 8. Either decreasing J or increasing D can transfer the system from an under-damped state to an over-damped one, which will enhance the stability of the system. It should be noted that the value of J cannot be too small so as to ensure that the BDFIG could provide sufficient inertia to the AC grid.

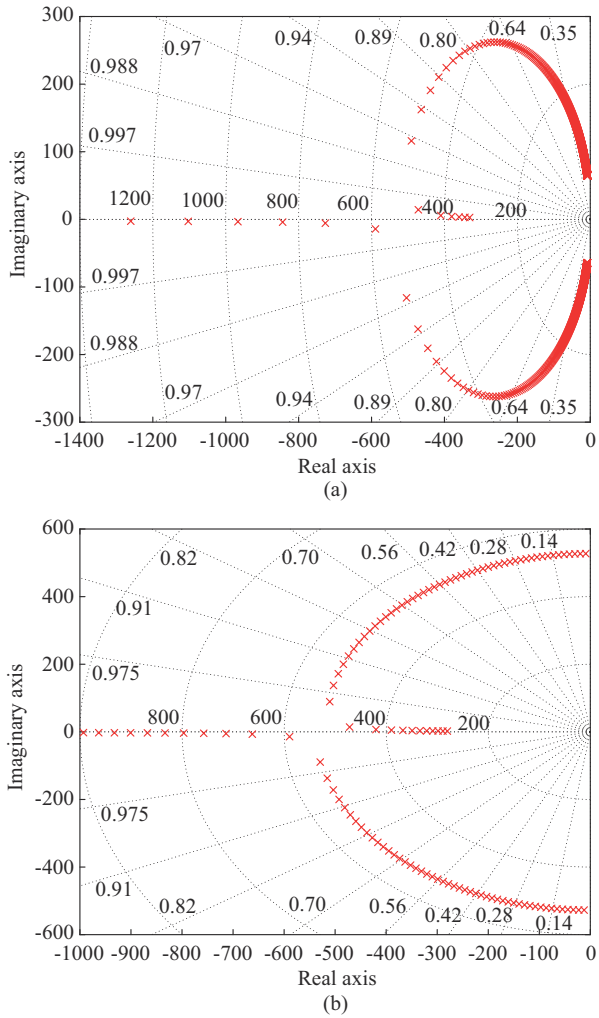

Fig. 8. Root trajectories under different J and D. (a) $J=0.1$ kg·m² and D is within [1,20]N·m·s/rad. (b) J is within [0.05,0.2]kg·m² and $D=10$ N·m·s/rad.

To analyze the effect of control parameters on the stability of the BDFIG system, the generalized Nyquist curves under different VSynC parameters are given in Fig. 9. From Fig. 9(a), it can be observed that as D increases, the generalized Nyquist curves no longer encircle the (–1, j0). From Fig. 9 (b), it can be observed that as J increases, the generalized Nyquist curves gradually encircle (–1, j0). In summary, increasing the virtual damping coefficient D will enhance the stability of the system. In contrast, increasing J will deteriorate the stability of the BDFIG system.

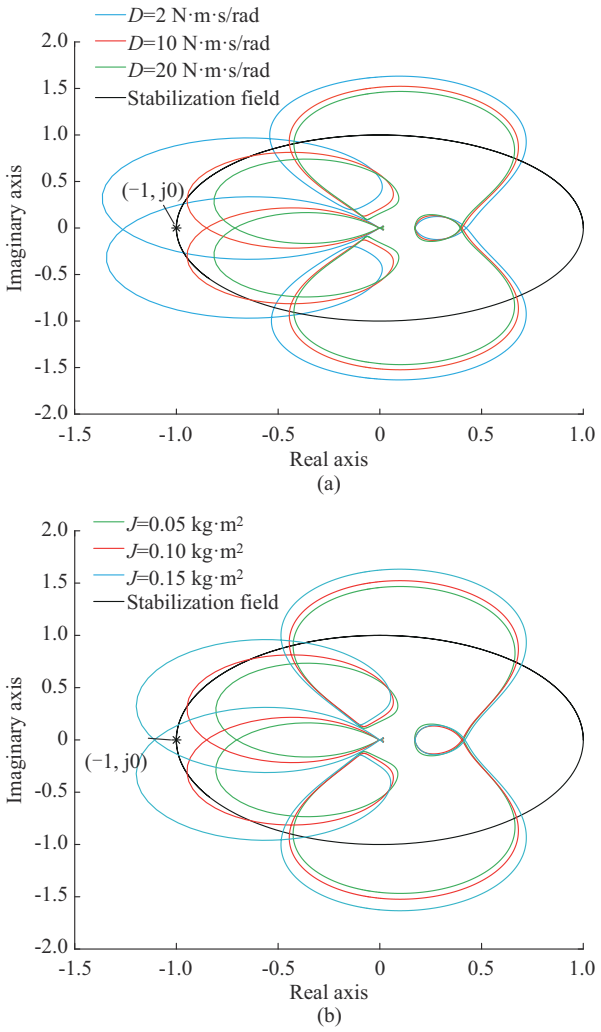

Fig. 9. Generalized Nyquist curves under different VSynC parameters. (a) $J=0.1$ kg·m^2. (b) $D=10$ N·m·s/rad.

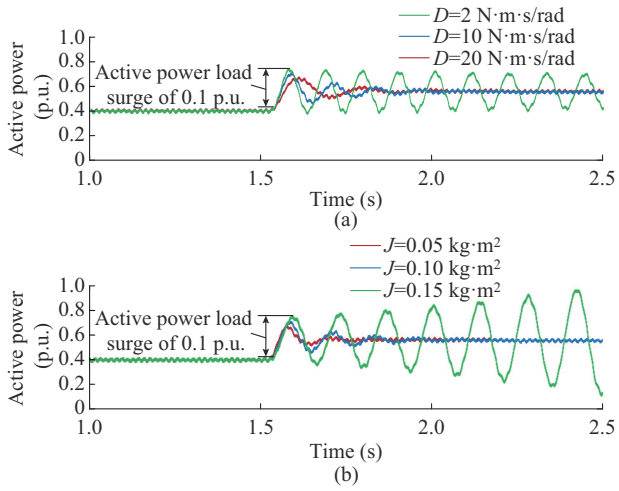

Fig. 10. Power response under different VSynC parameters. (a) $J=0.1$ kg·m^2. (b) $D=10$ N·m·s/rad.

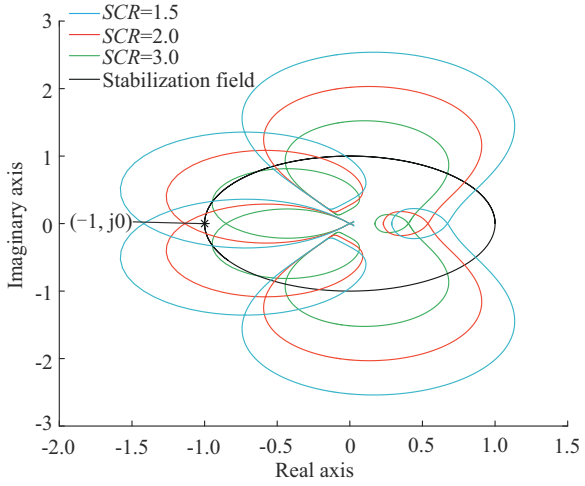

Fig. 11. Generalized Nyquist curves under different SCRs.

The power response of the BDFIG system under different VSynC parameters is shown in Fig. 10 and the simulation parameters are shown in Appendix B Table BI. In Fig. 10(a), the active power gets oscillated when $D=2$ N·m·s/rad, which is consistent with the theoretical analysis in Fig. 9(a). As D increases, the damping ratio of the BDFIG system gets increased, while the overshoot value becomes decreased. In Fig. 10(b), when $J=0.15$ kg·m^2, the active power gets oscillated, indicating that the BDFIG system cannot maintain stable operation, which is also consistent well with the theoretical analysis in Fig. 9(b). As J decreases, ξ gets increased. Consequently, the dynamic response time of the BDFIG system becomes short.

B. Influence Law of Grid Strength

The generalized Nyquist curves under different SCRs are shown in Fig. 11 with $D=10$ N·m·s/rad and $J=0.1$ kg·m^2. The generalized Nyquist curves do not wrap around (–1, j0) when $SCR=3.0$. However, as SCR decreases to 2.0 and 1.5, the generalized Nyquist curves get to wrap around (–1, j0), which indicates that the BDFIG system gets into an unstable state.

To validate the truth of the theoretical analysis, simulations under different SCRs are carried out. The results of electromagnetic transient simulation waveforms of BDFIG under different SCRs are presented in Fig. 12.

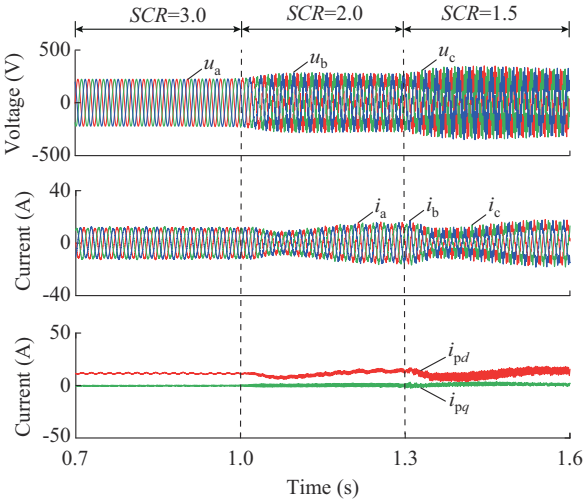

Fig. 12. Electromagnetic transient simulation waveforms of BDFIG system under different SCRs.

At the beginning, *SCR* = 3.0, at which time the BDFIG system can operate stably. Nevertheless, when *SCR* drops to 2.0 at 1.0 s, the voltage and current waveforms get to oscillate and the BDFIG system is destabilized. Further, when *SCR* drops to 1.5 at 1.3 s, the BDFIG system oscillates more obviously, which validates the theoretical analysis results in Fig. 11.

IV. Stability Enhanced Control Based on LADRC

A. LADRC-based Voltage and Current Inner Loop Design

The LADRC can significantly enhance the stability of the BDFIG system compared with the traditional PI control under the same bandwidth condition [26]-[28]. Therefore, the first-order LADRC is adopted to substitute the traditional controller in the voltage and current control loop. The control topology of BDFIG system based on LADRC is shown in Fig. 13.

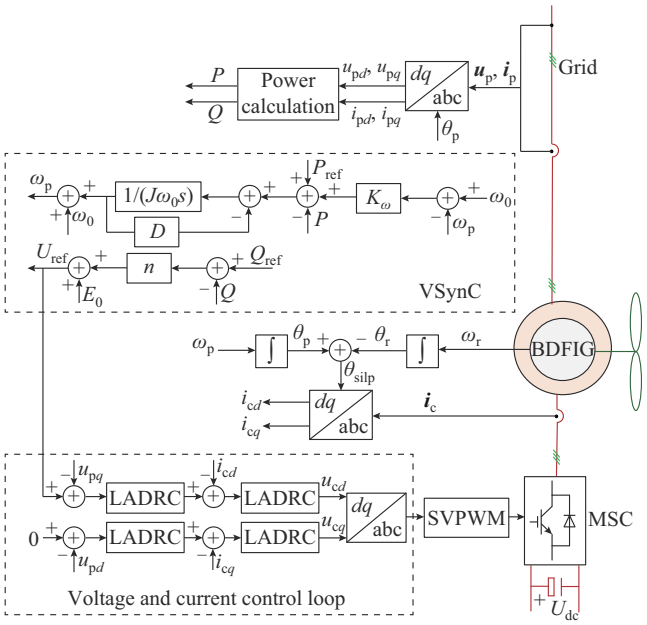

Fig. 13. Control topology of BDFIG system based on LADRC.

The structure of first-order LADRC is presented in Fig. 14, including the linear state error feedback (LSEF), linear extended state observer (LESO), and controlled object G_p.

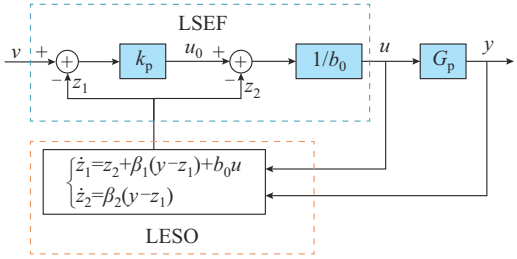

Fig. 14. Structure of first-order LADRC.

The LESO enables real-time observation of the actual BDFIG system, which can be deduced as:

$$\begin{cases} \dot{z}_1 = z_2 + \beta_1 (y - z_1) + b_0 u \\ \dot{z}_2 = \beta_2 (y - z_1) \end{cases} \tag{26}$$

The LSEF can increase the feedback amount based on the proportional control, which is conducive to enhancing the transient response of BDFIG system. The LSEF can be expressed as:

$$\begin{cases} u_0 = k_p (v - z_1) \\ u = \dfrac{1}{b_0} (u_0 - z_2) \end{cases} \tag{27}$$

The structure of single-parameter LADRC is applied, with ω_L symbolizing its bandwidth. Then, β_1, β_2, and k_p are exhibited as:

$$\begin{cases} k_p = \omega_L \\ \beta_1 = 2\omega_L \\ \beta_2 = \omega_L^2 \end{cases} \tag{28}$$

Further, based on (26) and (27), the equivalent topology of first-order LADRC is deduced, as shown in Fig. 15.

$$\begin{cases} C_1(s) = \dfrac{(\beta_2 + k_p\beta_1)s + k_p\beta_2}{(s + \beta_1 + k_p)b_0 s} = \\ \qquad \left(\dfrac{\beta_2 + k_p\beta_1}{b_0} + \dfrac{k_p\beta_2}{b_0 s}\right)\dfrac{1}{s + \beta_1 + k_p} \\ C_f(s) = \dfrac{k_p(s^2 + \beta_1 s + \beta_2)}{(\beta_2 + k_p\beta_1)s + k_p\beta_2} \end{cases} \tag{29}$$

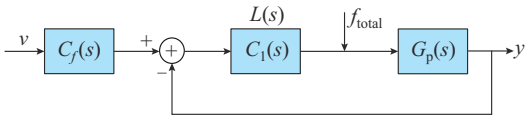

Fig. 15. Equivalent topology of first-order LADRC.

From (29), it can be concluded that $C_1(s)$ is equivalent to the combination of "a PI controller" plus "a first-order low-pass filter". Note that the numerator order of the equivalent of $C_f(s)$ is higher than that of the denominator, implying the achievement of phase compensation. This is why the LADRC behaves better in enhancing the stability of the-BDFIG system than that of the traditional PI control.

The design for the voltage and current control loops is given as follows. Considering symmetry, only the *d*-axis design process is presented.

The input reference of current control loop is the *d*-axis CW current $i_{cd,ref}$, while the feedback is the *d*-axis CW current i_{cd}. And the output is the *d*-axis CW voltage u_{cd}. The relationship can be expressed as:

$$\begin{cases} u_{cd} = R_c i_{cd} + \left(L_c - \dfrac{M_{cr}^2 L_p}{M_{pr} L_M}\right)\dot{i}_{cd} + \Delta u_{cd} \\ \dot{i}_{cd} = \dfrac{u_{cd} - R_c i_{cd} - \Delta u_{cd}}{L_c - \dfrac{M_{cr}^2 L_p}{M_{pr} L_M}} \end{cases} \tag{30}$$

According to (26), (27), and (30), the current loop can be designed as:

$$\begin{cases} y_{\mathrm{i}} = i_{cd} \\ u_{\mathrm{i}} = u_{cd} \\ r = i_{cd,\mathrm{ref}} \\ b_{0,i} = \dfrac{R_{\mathrm{c}}}{L_{\mathrm{c}} - \dfrac{M_{\mathrm{cr}}^2 L_{\mathrm{p}}}{M_{\mathrm{pr}} L_{\mathrm{M}}}} \end{cases} \tag{31}$$

Under the PW magnetic flux orientation, the changing rates of PW current and voltage can be approximated as a first-order linear relationship. Thus, the relationships between the PW and CW currents are exhibited as:

$$\begin{cases} i_{cd} = \dfrac{R_{\mathrm{r}} L_{\mathrm{p}}}{\omega_{\mathrm{p}} M_{\mathrm{cr}} M_{\mathrm{pr}}} i_{pq} - \dfrac{L_{\mathrm{M}}}{\omega_{\mathrm{p}} M_{\mathrm{cr}}} \dot{i}_{pq} + \Delta i_{cd} \\ \dot{i}_{pq} = \dfrac{\omega_{\mathrm{p}} M_{\mathrm{cr}}}{L_{\mathrm{M}}} i_{cd} + \dfrac{R_{\mathrm{r}} L_{\mathrm{p}}}{L_{\mathrm{M}} M_{\mathrm{pr}}} i_{pq} - \dfrac{\omega_{\mathrm{p}} M_{\mathrm{cr}}}{L_{\mathrm{M}}} \Delta i_{cd} \end{cases} \tag{32}$$

According to (26), (27), and (31), the voltage control loop can be designed as:

$$\begin{cases} y_{\mathrm{i}} = u_{pq} \\ u_{\mathrm{i}} = i_{cd} \\ r = u_{pq,\mathrm{ref}} \\ b_{0,\mathrm{u}} = \dfrac{\omega_{\mathrm{p}} M_{\mathrm{cr}}}{L_{\mathrm{M}}} \end{cases} \tag{33}$$

B. Stability Analysis of BDFIG System with LADRC

The generalized Nyquist curves of the BDFIG system under different SCRs and control methods are demonstrated in Fig. 16. The SCRs are set to be 3.0, 2.0, and 1.5, respectively. J and D take the values of 0.1 kg·m^2 and 10 N·m·s/rad, respectively. Three control methods are compared, i. e., the full PI (Method I), only the voltage loop with LADRC (Method II), and both the voltage and current control loops with LADRC (Method III).

As demonstrated in Fig. 16(a), the BDFIG system maintains stable when $SCR = 3.0$ under all the three control methods. From Fig. 16(b), when $SCR = 2.0$, only Methods II and III can keep the BDFIG system stable, when $SCR = 2.0$. From Fig. 16(c), only Method III can achieve a stable state. The simulation waveforms of BDFIG system under different SCRs and control methods are shown in Fig. 17.

Under weak grid condition, when Method I is used, the voltage and current of BDFIG system are destabilized. However, when Method II is utilized, the instability phenomenon gets enhanced to some extent, but instability phenomenon still exists when SCR goes down to 1.5. When Method III is triggered, the BDFIG system maintains stable even when $SCR = 1.5$, which is consistent with Fig. 16. In summary, Method III can virtually stretch the stable operation interval of the BDFIG system under weak grid condition.

V. Experimental Verification

To further verify the accuracy of the analysis, a 3 kW BDFIG experimental platform is built, as depicted in Fig. 18. The detailed specifications are listed in Appendix B Table BII. In the experiments, at the beginning of the operation, a pre-synchronous control is adopted in the BDFIG system. The dynamic response of the active power with different J and D is investigated firstly.

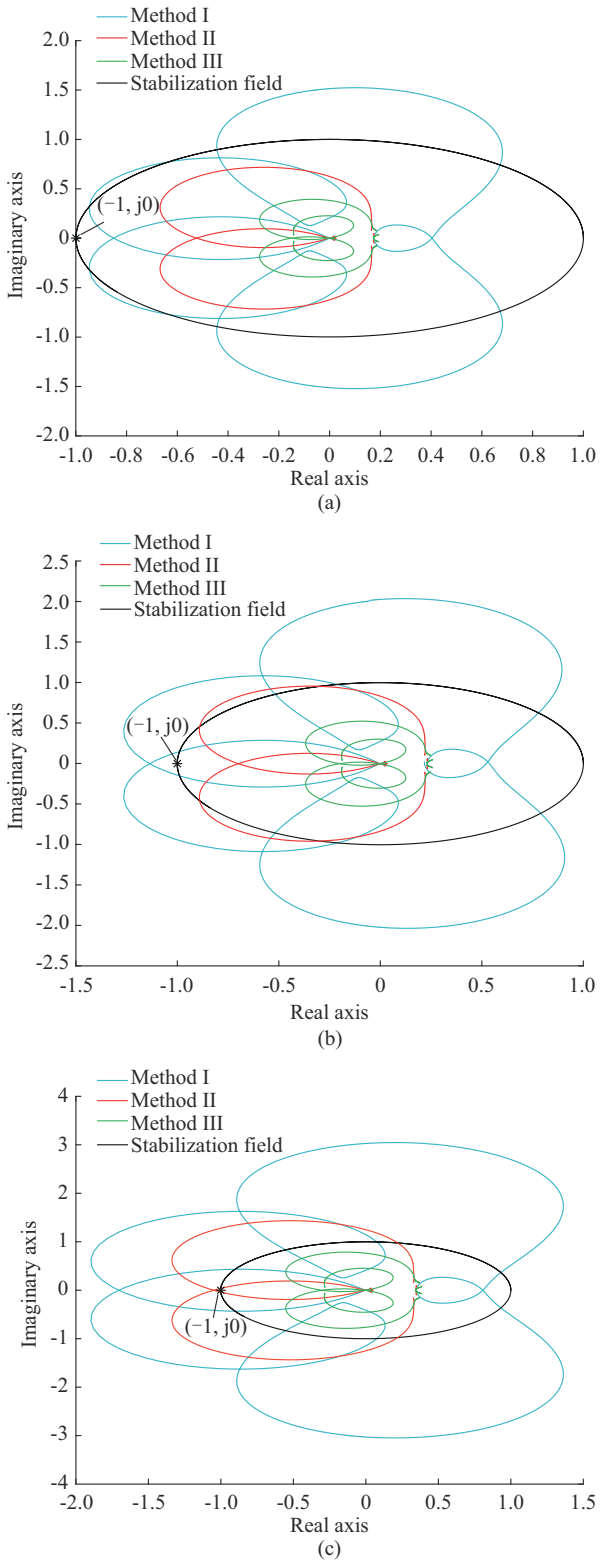

Fig. 16. Generalized Nyquist curves of BDFIG system under different SCRs and control methods. (a) $SCR = 3.0$. (b) $SCR = 2.0$. (c) $SCR = 1.5$.

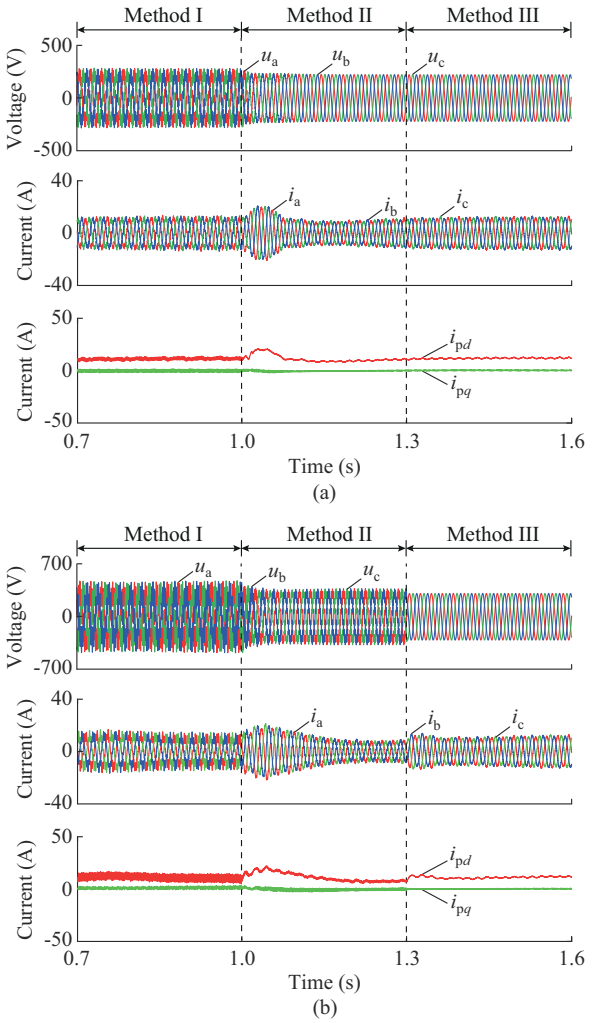

Fig. 17. Simulation waveforms of BDFIG system under different SCRs and control methods. (a) $SCR=2.0$. (b) $SCR=1.5$.

The experimental results of power step response of the BDFIG system under different VSynC parameters are shown in Fig. 19. As observed in Fig. 19(a), an increase in D results in a reduction in system overshoot and a shorter transition period. Conversely, Fig. 19(b) indicates that higher D values lead to larger system overshoot values. Note that when $J=0.2$ kg·m^2, the active power exhibits oscillation, suggesting that the BDFIG system struggles to maintain stable operation under these conditions.

Experimental results with traditional PI control under different SCRs are shown in Fig. 20. When $SCR=3.0$, the BDFIG system can operate stably with a total harmonic distortion (THD) of 3.87% of the PW current. When SCR decreases to 2.0 and 1.5, the voltage and current waveforms become distorted with $THD=10.09\%$ and $THD=12.43\%$, respectively. It can be concluded that as SCR decreases, the BDFIG system tends to be unstable. In theory, high THD indicates a decrease in the stability of the BDFIG system, especially for nonlinear BDFIG systems, such as power electronic converters [29], [30].

The experimental results with enhanced VSynC method under different SCRs are shown in Fig. 21. When $SCR=2.0$ and $SCR=1.5$, compared with the traditional PI control, THD get enhanced significantly, i.e., reduced from 10.09% to 4.76% and reduced from 12.43% to 5.05%, respectively. In conclusion, the enhanced VSynC method is much beneficial in inhibiting the instability phenomenon.

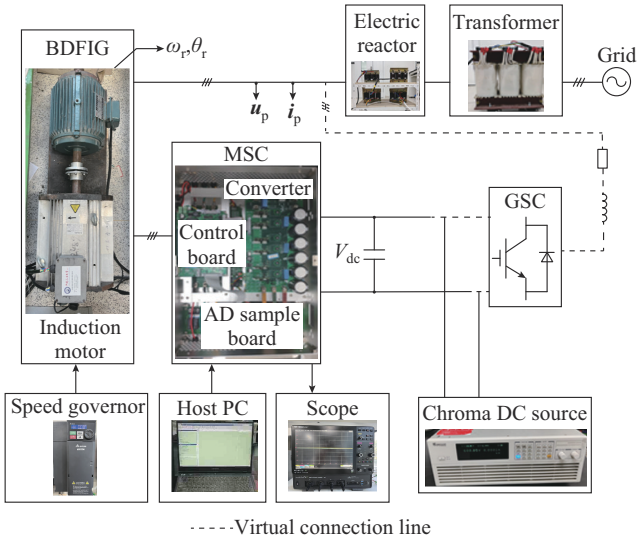

Fig. 18. Experimental platform of BDFIG.

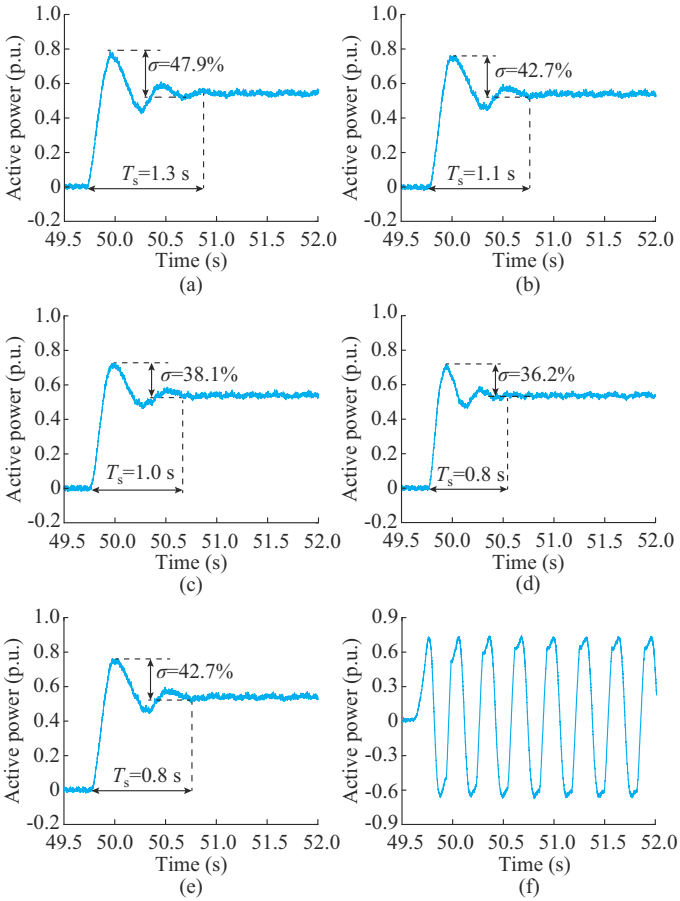

Fig. 19. Experimental results of BDFIG system power step response under different VSynC parameters. (a) $D=2$ N·m·s/rad, $J=0.1$ kg·m^2. (b) $D=5$ N·m·s/rad, $J=0.1$ kg·m^2. (c) $D=10$ N·m·s/rad, $J=0.1$ kg·m^2. (d) $D=5$ N·m·s/rad, $J=0.05$ kg·m^2. (e) $D=5$ N·m·s/rad, $J=0.1$ kg·m^2. (f) $D=5$ N·m·s/rad, $J=0.2$ kg·m^2.

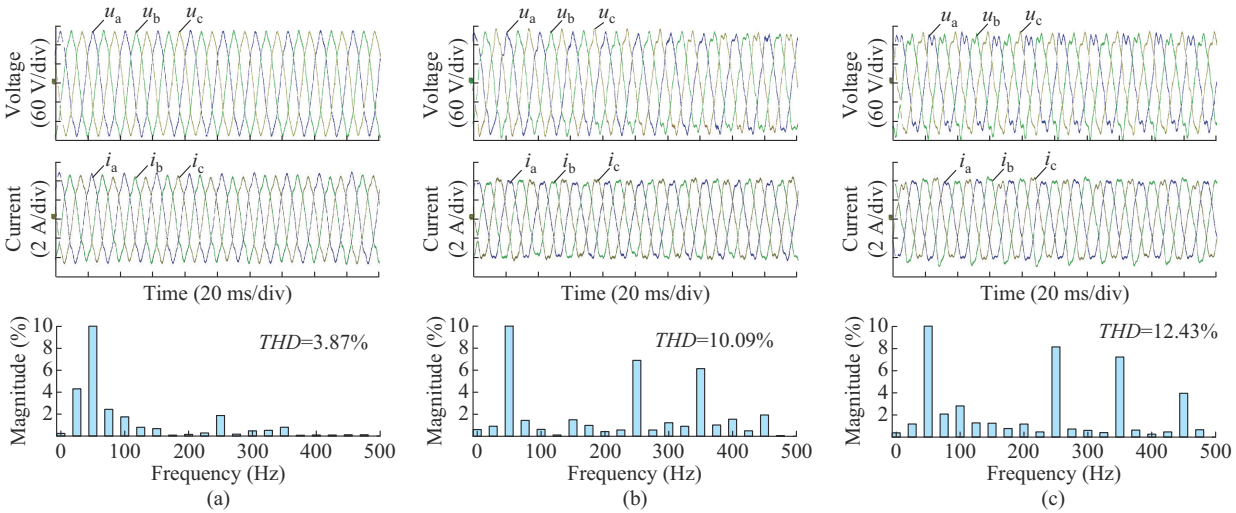

Fig. 20. Experimental results with traditional PI control method under different SCRs. (a) $SCR = 3.0$. (b) $SCR = 2.0$. (c) $SCR = 1.5$.

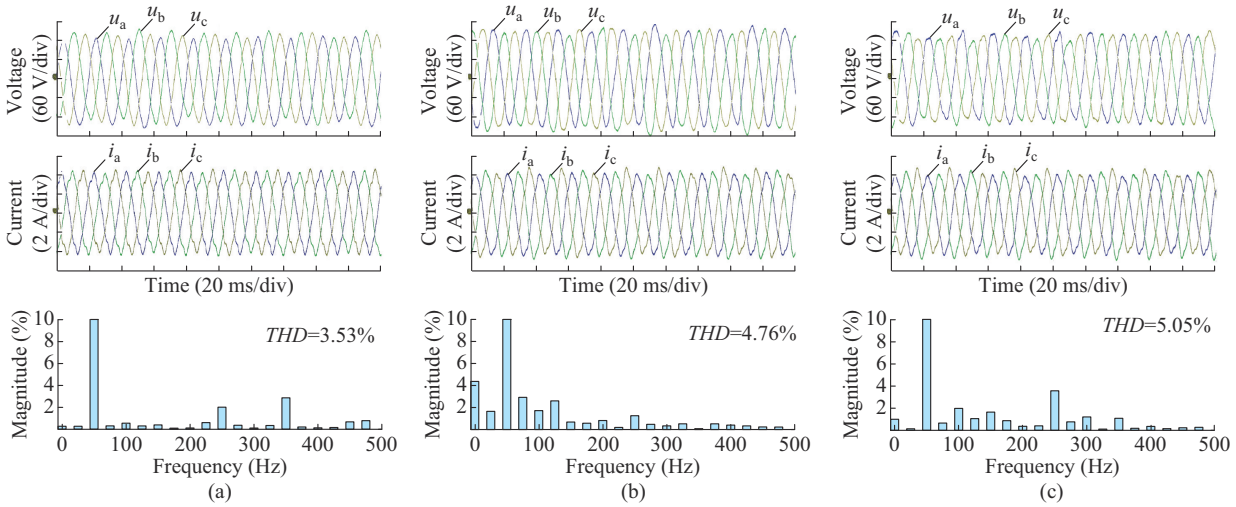

Fig. 21. Experimental results with enhanced VSynC method under different SCRs. (a) $SCR = 3.0$. (b) $SCR = 2.0$. (c) $SCR = 1.5$.

The experimental results under different speeds are shown in Fig. 22. When $SCR = 1.5$, the enhanced VSynC method is utilized. The rated speed of BDFIG is 750 r/min. From Fig. 22, when the BDFIG is running under super-synchronous operation mode (850 r/min) and sub-synchronous operation mode (650 r/min), the enhanced VSynC method can make the BDFIG system keep stable operation. It means that the enhanced VSynC method cannot be affected by the operation speed of the BDFIG system.

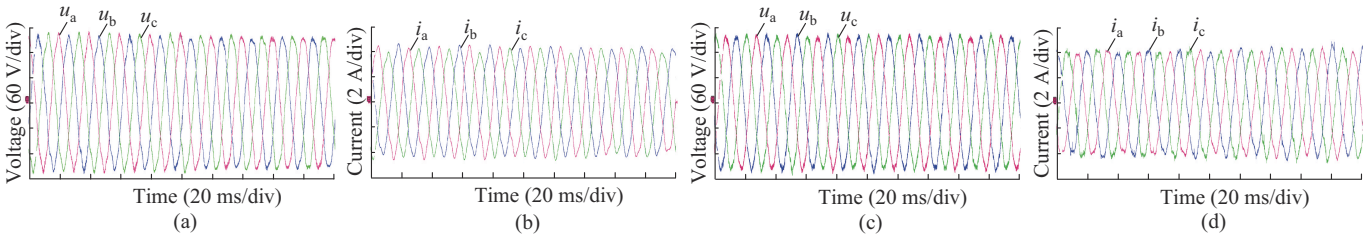

Fig. 22. Experimental results under different speeds. (a) PW voltage under sub-synchronous operation mode. (b) PW current under sub-synchronous operation mode. (c) PW voltage under super-synchronous operation mode. (d) PW current under super-synchronous operation mode.

VI. Conclusion

In this paper, the admittance model of BDFIG with VSynC is constructed. Furthermore, an enhanced VSynC method based on LADRC is proposed to enhance the stability of the BDFIG system under weak grid condition. The specific conclusions are summarized as follows.

1) Based on the established BDFIG model, the VSynC loop mainly changes the impedance characteristics of the BDFIG in low frequency band, while it has almost no effect on the middle and high frequency bands.

2) J and D have significant influence on the stability of the BDFIG system, i.e., increasing D can enhance the stability margin, while increasing J can reduce the stability margin.

3) The proposed method can significantly enhance the stability of the BDFIG system with a simple structure.

The influence of the LADRC on the BDFIG transient characteristics remains to be evaluated, which will be studied in the near future.

APPENDIX A

$$\begin{cases} \boldsymbol{u}_{\mathrm{p}} = R_{\mathrm{p}}\boldsymbol{i}_{\mathrm{p}} + p\boldsymbol{\psi}_{\mathrm{p}} + \mathrm{j}\omega_{\mathrm{p}}\boldsymbol{\psi}_{\mathrm{p}} \\ \boldsymbol{u}_{\mathrm{c}} = R_{\mathrm{c}}\boldsymbol{i}_{\mathrm{c}} + p\boldsymbol{\psi}_{\mathrm{c}} + \mathrm{j}\omega_{\mathrm{c}}\boldsymbol{\psi}_{\mathrm{c}} \\ \boldsymbol{u}_{\mathrm{r}} = R_{\mathrm{r}}\boldsymbol{i}_{\mathrm{r}} + p\boldsymbol{\psi}_{\mathrm{r}} + \mathrm{j}\omega_{\mathrm{r}}\boldsymbol{\psi}_{\mathrm{r}} \end{cases} \tag{A1}$$

$$\begin{cases} \boldsymbol{G}_{\mathrm{ipp}} = \begin{bmatrix} a_1 & a_2 \\ -a_2 & a_1 \end{bmatrix} \\ \boldsymbol{G}_{\mathrm{pr}} = \begin{bmatrix} -a_3 & a_4 \\ -a_4 & -a_3 \end{bmatrix} \end{cases} \tag{A2}$$

$$\begin{cases} \boldsymbol{G}_{\mathrm{icc}} = \begin{bmatrix} b_1 & b_2 \\ -b_2 & b_1 \end{bmatrix} \\ \boldsymbol{G}_{\mathrm{cr}} = \begin{bmatrix} -b_3 & b_4 \\ -b_4 & -b_3 \end{bmatrix} \end{cases} \tag{A3}$$

$$\begin{cases} a_1 = k_{\mathrm{a}}(R_{\mathrm{p}} + sL_{\mathrm{p}}) \\ a_2 = k_{\mathrm{a}}\omega_{\mathrm{p}}L_{\mathrm{p}} \\ a_3 = k_{\mathrm{a}}[(R_{\mathrm{p}} + sL_{\mathrm{p}})sM_{\mathrm{pr}} + \omega_{\mathrm{p}}^2 L_{\mathrm{p}}M_{\mathrm{pr}}] \\ a_4 = k_{\mathrm{a}}R_{\mathrm{p}}\omega_{\mathrm{p}}M_{\mathrm{pr}} \\ k_{\mathrm{a}} = \dfrac{1}{(R_{\mathrm{p}} + sL_{\mathrm{p}})^2 + (\omega_{\mathrm{p}}L_{\mathrm{p}})^2} \end{cases} \tag{A4}$$

$$\begin{cases} b_1 = k_{\mathrm{b}}(R_{\mathrm{c}} + sL_{\mathrm{c}}) \\ b_2 = k_{\mathrm{b}}\omega_{\mathrm{c}}L_{\mathrm{c}} \\ b_3 = k_{\mathrm{b}}[(R_{\mathrm{c}} + sL_{\mathrm{c}})sM_{\mathrm{cr}} + \omega_{\mathrm{c}}^2 L_{\mathrm{c}}M_{\mathrm{cr}}] \\ b_4 = k_{\mathrm{b}}R_{\mathrm{c}}\omega_{\mathrm{c}}M_{\mathrm{cr}} \\ k_{\mathrm{b}} = \dfrac{1}{(R_{\mathrm{c}} + sL_{\mathrm{c}})^2 + (\omega_{\mathrm{c}}L_{\mathrm{c}})^2} \end{cases} \tag{A5}$$

$$\begin{cases} \boldsymbol{G}_{\mathrm{irp}} = \begin{bmatrix} e_1 & e_2 \\ -e_2 & e_1 \end{bmatrix} \\ \boldsymbol{G}_{\mathrm{rc}} = \begin{bmatrix} e_3 & -e_4 \\ e_4 & e_3 \end{bmatrix} \end{cases} \tag{A6}$$

$$\begin{cases} c_1 = \dfrac{M_{\mathrm{cr}}}{M_{\mathrm{pr}}} \\ c_2 = \dfrac{\omega_{\mathrm{r}}}{s^2 + \omega_{\mathrm{r}}^2}\dfrac{R_{\mathrm{r}}}{M_{\mathrm{pr}}} \\ c_3 = \dfrac{L_{\mathrm{r}}}{M_{\mathrm{pr}}} + \dfrac{s}{s^2 + \omega_{\mathrm{r}}^2}\dfrac{R_{\mathrm{r}}}{M_{\mathrm{pr}}} \end{cases} \tag{A7}$$

$$\begin{cases} d_1 = c_1(R_{\mathrm{p}} + sL_{\mathrm{p}}) \\ d_2 = c_1\omega_{\mathrm{p}}L_{\mathrm{p}} \\ d_3 = sM_{\mathrm{pr}} - c_2\omega_{\mathrm{p}}L_{\mathrm{p}} - c_3(R_{\mathrm{p}} + sL_{\mathrm{p}}) \\ d_4 = c_2(R_{\mathrm{p}} + sL_{\mathrm{p}}) - c_3\omega_{\mathrm{p}}L_{\mathrm{p}} + \omega_{\mathrm{p}}M_{\mathrm{pr}} \end{cases} \tag{A8}$$

$$\begin{cases} k_{\mathrm{e}} = \dfrac{1}{d_3^2 + d_4^2} \\ e_1 = k_{\mathrm{e}}d_3 \\ e_2 = k_{\mathrm{e}}d_4 \\ e_3 = k_{\mathrm{e}}(d_2d_4 - d_1d_3) \\ e_4 = k_{\mathrm{e}}(d_1d_4 + d_2d_3) \end{cases} \tag{A9}$$

In calculating open-loop input admittance model of BDFIG, Fig. 2 is simplified to the following form and (6) can be obtained from Fig. A1.

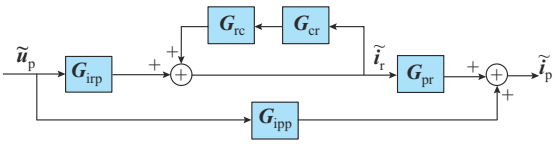

Fig. A1. Simplified open-loop input admittance model of BDFIG system.

APPENDIX B

In the synchronous coordinate system, the active and reactive power references of PWs during steady state are $P_{\mathrm{p,ref}}$ and $Q_{\mathrm{p,ref}}$, respectively. Equation (12) is obtained by introducing a small-signal disturbance at the steady-state working point.

$$\begin{cases} P_{\mathrm{p,ref}} = -\dfrac{3(I_{pd}U_{pd} + I_{pq}U_{pq})}{2} \\ Q_{\mathrm{p,ref}} = -\dfrac{3(I_{pd}U_{pq} - I_{pq}U_{pd})}{2} \end{cases} \tag{B1}$$

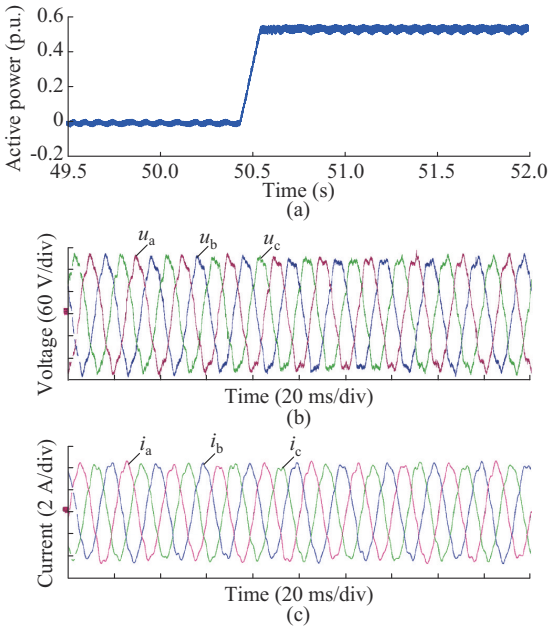

Fig. B1. Experimental results of power step response without VSynC ($SCR = 3.0$). (a) Waveforms of active power dynamic response. (b) Waveforms of PW voltage. (c) Waveforms of PW current.

TABLE BI
SIMULATION PARAMETERS

Parameter	Value
U_g (V)	380
R_p (p.u.)	0.067
R_c (p.u.)	0.073
R_r (p.u.)	0.130
L_p (p.u.)	24.510
L_c (p.u.)	2.660
L_r (p.u.)	27.250
M_{pr} (p.u.)	24.280
M_{cr} (p.u.)	2.540

TABLE BII
EXPERIMENTAL PARAMETERS OF 3 kW BDFIG SYSTEM

Parameter	Value
P_{ref} (kW)	3
U_g (V)	380
P_p	3
P_c	1
R_p (Ω)	3.200
R_c (Ω)	5.320
R_r (mΩ)	0.130
L_p (H)	0.292
L_c (H)	0.642
L_r (mH)	0.048
M_{pr} (mH)	2.160
M_{cr} (mH)	4.000

REFERENCES

[1] R. McMahon, P. Tavner, E. Abdi *et al.*, "Characterizing brushless doubly fed machine rotors," *IET Electric Power Applications*, vol. 7, no. 7, pp. 535-876, Aug. 2013.

[2] P. Mukherjee and V. V. Rao, "Superconducting magnetic energy storage for stabilizing grid integrated with wind power generation systems," *Journal of Modern Power Systems and Clean Energy*, vol. 7, no. 2, pp. 400-411, Mar. 2019.

[3] T. Long, S. Shao, P. Malliband *et al.*, "Crowbar-less fault ride-through of the brushless doubly fed induction generator in a wind turbine under symmetrical voltage dips," *IEEE Transactions on Industrial Electronics*, vol. 60, no. 7, pp. 2833-2841, Jul. 2013.

[4] Y. Wang, H. Xu, P. Ge *et al.*, "Stability estimation and enhanced control of BDFIG-driven wind turbines under weak grid," in *Proceedings of 2023 3rd New Energy and Energy Storage System Control Summit Forum (NEESSC)*, Mianyang, China, Sept. 2023, pp. 243-249.

[5] C. Wang, H. Xu, P. Ge *et al.*, "Transient stability analysis and enhancement for BDFIG based virtual synchronous control," in *Proceedings of 2023 3rd New Energy and Energy Storage System Control Summit Forum (NEESSC)*, Mianyang, China, Sept. 2023, pp. 259-263.

[6] A. Nair, S. Kamalasadan, J. Geis-Schroer *et al.*, "An investigation of grid stability and a new design of adaptive phase-locked loop for wind-integrated weak power grid," *IEEE Transactions on Industry Applications*, vol. 58, no. 5, pp. 5871-5884, Sept. 2022.

[7] L. Xiong, P. Li, F. Wu *et al.*, "Stability enhancement of power systems with high DFIG-wind turbine penetration via virtual inertia planning," *IEEE Transactions on Power Systems*, vol. 34, no. 2, pp. 1352-1361, Mar. 2019.

[8] J. Liu, W. Yao, J. Wen *et al.*, "Impact of power grid strength and PLL parameters on stability of grid-connected DFIG wind farm," *IEEE Transactions on Sustainable Energy*, vol. 11, no. 1, pp. 545-557, Jan. 2020.

[9] P. Chen, C. Qi, and X. Chen, "Virtual inertia estimation method of DFIG-based wind farm with additional frequency control," *Journal of Modern Power Systems and Clean Energy*, vol. 9, no. 5, pp. 1076-1087, Sept. 2021.

[10] V. Nayanar, N. Kumaresan, and N. A. Gounden, "A single-sensor-based MPPT controller for wind-driven induction generators supplying DC microgrid," *IEEE Transactions on Power Electronics*, vol. 31, no. 2, pp. 1161-1172, Feb. 2016.

[11] R. Peña-Alzola, D. Campos-Gaona, P. F. Ksiazek *et al.*, "DC-link control filtering options for torque ripple reduction in low-power wind Turbines," *IEEE Transactions on Power Electronics*, vol. 32, no. 6, pp. 4812-4826, Jun. 2017.

[12] W. Du, W. Dong, Y. Wang *et al.*, "Small-disturbance stability of a wind farm with virtual synchronous generators under the condition of weak grid connection," *IEEE Transactions on Power Systems*, vol. 36, no. 6, pp. 5500-5511, Nov. 2021.

[13] N. Mohammed, M. H. Ravanji, W. Zhou *et al.*, "Online grid impedance estimation-based adaptive control of virtual synchronous generators considering strong and weak grid conditions," *IEEE Transactions on Sustainable Energy*, vol. 14, no. 1, pp. 673-687, Jan. 2023.

[14] S. Wang, J. Hu, and X. Yuan, "Virtual synchronous control for grid-connected DFIG-based wind turbines," *IEEE Journal of Emerging and Selected Topics in Power Electronics*, vol. 3, no. 4, pp. 932-944, Dec. 2015.

[15] L. Shang, J. Hu, X. Yuan *et al.*, "Improved virtual synchronous control for grid-connected VSCs under grid voltage unbalanced conditions," *Journal of Modern Power Systems and Clean Energy*, vol. 7, no. 1, pp. 174-185, Jan. 2019.

[16] S. Wang, J. Hu, X. Yuan *et al.*, "On inertial dynamics of virtual-synchronous-controlled DFIG-based wind turbines," *IEEE Transactions on Energy Conversion*, vol. 30, no. 4, pp. 1691-1702, Dec. 2015.

[17] H. Nian and Y. Jiao, "Improved virtual synchronous generator control of DFIG to ride-through symmetrical voltage fault," *IEEE Transactions on Energy Conversion*, vol. 35, no. 2, pp. 672-683, Jun. 2020.

[18] H. Shao, X. Cai, Z. Li *et al.*, "Stability enhancement and direct speed control of DFIG inertia emulation control strategy," *IEEE Access*, vol. 7, pp. 120089-120105, Aug. 2019.

[19] C. Li, Y. Yang, Y. Cao *et al.*, "Frequency and voltage stability analysis of grid-forming virtual synchronous generator attached to weak grid," *IEEE Journal of Emerging and Selected Topics in Power Electronics*, vol. 10, no. 3, pp. 2662-2671, Jun. 2022.

[20] H. Xu, F. Nie, Z. Wang *et al.*, "Impedance modeling and stability factor assessment of grid-connected converters based on linear active disturbance rejection control," *Journal of Modern Power Systems and Clean Energy*, vol. 9, no. 6, pp. 1327-1338, Nov. 2021.

[21] Z. Xie, Y. Chen, W. Wu *et al*., "Admittance modeling and stability analysis of grid-connected inverter with LADRC-PLL," *IEEE Transactions on Industrial Electronics*, vol. 68, no. 12, pp. 12272-12284, Dec. 2021.

[22] H. Liu, F. Bu, W. Huang *et al*., "Linear active disturbance rejection control for dual-stator winding induction generator AC power system," *IEEE Transactions on Industrial Electronics*, vol. 70, no. 7, pp. 6597-6607, Jul. 2023.

[23] S. Shao, E. Abdi, F. Barati *et al.*, "Stator-flux-oriented vector control for brushless doubly fed induction generator," *IEEE Transactions on Industrial Electronics*, vol. 56, no. 10, pp. 4220-4228, Oct. 2009.

[24] X. Yan and M. Cheng, "Backstepping-based direct power control for dual-cage rotor brushless doubly fed induction generator," *IEEE Transactions on Power Electronics*, vol. 38, no. 2, pp. 2668-2680, Feb. 2023.

[25] M. Lu, Y. Chen, D. Zhang *et al.*, "Virtual synchronous control based on control winding orientation for brushless doubly fed induction generator (BDFIG) wind turbines under symmetrical grid faults," *Energies*, vol. 12, no. 2, pp. 319-319, Jan. 2019.

[26] P. Lin, Z. Wu, Z. Fei *et al.*, "A generalized PID interpretation for high-order LADRC and cascade LADRC for servo systems," *IEEE Transactions Industrial Electronics*, vol. 69, no. 5, pp. 5207-5214, May 2022.

[27] R. Zhou, C. Fu, and W. Tan, "Implementation of linear controllers via active disturbance rejection control structure," *IEEE Transactions on Industrial Electronics*, vol. 68, no. 7, pp. 6217-6226, Jul. 2021.

[28] W. Ma, Y. Guan, and B. Zhang, "Active disturbance rejection control based control strategy for virtual synchronous generators," *IEEE Transactions on Energy Conversion*, vol. 35, no. 4, pp. 1747-1761, Dec. 2020.

[29] M. Zhu, Y. Ye, Y. Xiong *et al*., "Parameter robustness improvement for repetitive control in grid-tied inverters using an IIR filter," *IEEE Transactions on Power Electronics*, vol. 36, no. 7, pp. 8454-8463, Jul.

2021.
[30] W. Xu, O. M. E. Mohammed, Y. Liu *et al*., "Negative sequence voltage compensating for unbalanced standalone brushless doubly-fed induction generator," *IEEE Transactions on Power Electronics*, vol. 35, no. 1, pp. 667-680, Jan. 2020.

Hailiang Xu received the B.S. and Ph.D. degrees in electrical engineering from China University of Petroleum (East China), Qingdao, China, and Zhejiang University, Hangzhou, China, in 2008 and 2014, respectively. He is currently working as Professor with China University of Petroleum (East China). His current research interests include renewable energy generation and microgrid.

Chao Wang received the B.S. degree from the China University of Petroleum (East China), Qingdao, China, in 2022. He is currently pursuing the M. S. degree with the New Energy College, China University of Petroleum (East China), Qingdao, China. His current research interests include stability analysis and control of brushless doubly-fed induction generator systems.

Zhongxing Wang received the B.S. degree from the China University of Petroleum (East China), Qingdao, China, in 2020. He is currently pursuing the M.S. degree with the New Energy College, China University of Petroleum (East China). His current research interests include stability analysis and control of brushless doubly-fed induction generator systems.

Pingjuan Ge received the B.S. and Ph.D. degrees both in electrical engineering from Anhui University, Hefei, China, and Hunan University, Changsha, China, in 2017 and 2022, respectively. She is currently working as a Lecturer with China University of Petroleum (East China), Qingdao, China. Her current research interests include modeling and transient stability analysis of power-electronized power systems.

Rende Zhao received the B.S. and M.S. degrees in electrical engineering from Shandong University, Jinan, China, in 1999 and 2002, respectively, and the Ph.D. degree from the College of Electrical Engineering, Zhejiang University, Hangzhou, China, in 2005. Since 2006, he has been with the China University of Petroleum (East China), Qingdao, China, where he is currently a Full Professor. He was a Visiting Scholar with Aalborg University, Aalborg, Denmark, from 2015 to 2016. His research interests include renewable energy generation and motor control.